UC Santa Cruz
UC Santa Cruz Previously Published Works

Title

Enhanced Poleward Flux of Atmospheric Moisture to the Weddell Sea Region (ODP Site 690) During the Paleocene-Eocene Thermal Maximum

Permalink

https://escholarship.org/uc/item/8861w4f4

Journal

Paleoceanography and Paleoclimatology, 35(6)

ISSN

2572-4517

Authors

Kozdon, Reinhard
Penman, Donald E
Kelly, DC
et al.

Publication Date

2020-06-01

DOI

10.1029/2019pa003811

Peer reviewed

Kozdon Reinhard (Orcid ID: 0000-0001-6347-456X)
Penman Donald, E (Orcid ID: 0000-0003-4191-0505)
Zachos James, C (Orcid ID: 0000-0001-8439-1886)
Fournelle John H. (Orcid ID: 0000-0001-9689-8852)
Valley John W., W (Orcid ID: 0000-0003-3530-2722)

Enhanced Poleward Flux of Atmospheric Moisture to the Weddell Sea Region (ODP Site 690) during the Paleocene-Eocene Thermal Maximum

Reinhard Kozdon[1], Donald E. Penman[2], D. C. Kelly[3], J.C. Zachos[4], John. H. Fournelle[3], J. W. Valley[5]

[1] Lamont-Doherty Earth Observatory
[2] Department of Geology & Geophysics, Yale University
[3] Department of Geoscience, UW-Madison
[4] Department of Earth and Planetary Sciences, UC-Santa Cruz
[5] WiscSIMS, Department of Geoscience, UW-Madison

Abstract

Earth's hydrological cycle was profoundly perturbed by massive carbon emissions during an ancient (56 Ma) global warming event referred to as the Paleocene-Eocene thermal maximum (PETM). One approach to gaining valuable insight into the response of the hydrological cycle is to construct sea-surface salinity (SSS) records that can be used to gauge changes in the rates of evaporation and precipitation during the PETM in such climatically sensitive areas as the circum-Antarctic region. Here, we pair oxygen isotope ($\delta^{18}O$) and magnesium-calcium (Mg/Ca) measurements to reconstruct PETM sea-surface temperatures (SSTs) and $\delta^{18}O$ composition of seawater ($\delta^{18}O_{sw}$) at austral Site 690 (Weddell Sea). Several discrepancies emerge between the $\delta^{18}O$- and Mg/Ca-based SST records, with the latter indicating that the earliest PETM was punctuated by a short-lived ~4ºC increase in local SSTs. Conversion of the $\delta^{18}O_{sw}$ values to SSS reveals a ~4 ppt decrease ~50 ka after peak PETM warming at Site 690. This negative SSS ($\delta^{18}O_{sw}$) anomaly coincides with a prominent minimum in the planktic foraminifer $\delta^{18}O$ record published for the Site 690 PETM section. Thus, our revised interpretation posits that this $\delta^{18}O$ minimum signals a decrease in surface-ocean $\delta^{18}O_{sw}$ fostered by a transient increase in mean annual precipitation in the Weddell Sea region. The results of this study corroborate the view that the poleward flux of atmospheric moisture temporarily increased during a distinctive stage of the PETM.

(224/250 Words)

1. Introduction

The series of transient global warming events superimposed upon the long-term greenhouse climate state of the early Paleogene (~65–39 Ma) are geological analogs for gauging the future environmental consequences of unabated greenhouse gas emissions (e.g., Zachos et al., 2008; Zeebe et al., 2009; Zeebe and Zachos, 2013). The most prominent of these 'thermal maxima' occurred ~56 Ma (Zeebe and Lourens, 2019) and is referred to as the Paleocene-Eocene thermal maximum, or PETM. Hallmarks of the PETM in deep-sea records are abrupt decreases in the oxygen (δ^{18}O) and carbon isotope (δ^{13}C) compositions of foraminifer calcite (e.g., Kennett and Stott, 1991; Zachos et al., 2001), and a sharp decline in sedimentary calcite content (Dickens et al., 1997; Thomas et al., 1999). Together, these lines of evidence reflect ~4-5ºC of ocean warming coupled with a brief pulse of intense carbonate dissolution driven by the geologically rapid release of massive quantities of δ^{13}C-depleted carbon (e.g., Aze et al., 2014; Babila et al., 2016; Babila et al., 2018; DeConto et al., 2012; Dickens et al., 1995; Frieling et al., 2017; Higgins and Schrag, 2006; Jones et al., 2013; Penman et al., 2014; Svensen et al., 2004; Zachos et al., 2003; Zachos et al., 2005; Zachos et al., 2006; Zeebe et al., 2008).

The source(s) for carbon input during the PETM is debated (e.g., McInerney and Wing, 2011), but there is general consensus that many aspects of the PETM climatic and carbon cycle responses provide contextual constraints on ocean-climate change predicted to unfold in the coming centuries (Zeebe and Zachos, 2013). In theory, rising surface temperatures should accelerate and intensify the hydrological cycle (Clementz and Sewall, 2011; Held and Soden, 2000; 2006); hence, the greenhouse climate state of the PETM is thought to have been broadly associated with a more humid atmosphere (Bowen et al., 2004; Tipple et al., 2011). There is now a large body of evidence to indicate that the response of the hydrological cycle entailed a high degree of regional and temporal variability (Carmichael et al., 2017; Clechenko et al., 2007; Egger et al., 2003; Foreman et al., 2012; Handley et al., 2012; John et al., 2012; Kraus and Riggins, 2007; Larrasoaña et al., 2012; Pagani et al., 2006; Pujalte et al., 2019; Schmitz and Pujalte, 2007; Wing et al., 2005). Nonetheless, a first order feature of the PETM hydrological cycle that was more global in scope appears to have been an increase in meridional (equator-to-pole) transport of atmospheric water vapor (e.g., Huber and Goldner, 2012; Pagani et al., 2013; Pierrehumbert, 2002). Support for such an increase in poleward moisture transport is provided by micropaleontological and *n*-alkane hydrogen isotope records indicating reduced sea-surface salinities in the central Arctic Ocean during the PETM (Pagani et al., 2006; Sluijs et al., 2008).

In this study, we build upon the foundation laid by previous studies in an effort to better understand how the poleward flux of water vapor changed in response to rapid carbon input during the PETM. To this end, paired $\delta^{18}O$ and Mg/Ca ratios measured from planktic foraminifer shells are used to generate parallel records of sea-surface temperature (SST) and seawater oxygen isotope composition ($\delta^{18}O_{sw}$) for the PETM section recovered at Ocean Drilling Program (ODP) Site 690 (Fig. 1). This approach to reconstructing spatiotemporal variation in the hydrological cycle is predicated upon observed covariance between meridional gradients in surface $\delta^{18}O_{sw}$ and sea-surface salinity (SSS) in the modern ocean as both seawater properties are a function of differences in evaporation and precipitation (e.g., Schmitt, 1995). Culturing experiments have shown that the oxygen isotope composition of planktic foraminifer shells ($\delta^{18}O_{shell}$) is dependent upon both $\delta^{18}O_{sw}$ and calcification temperature (e.g., Bemis et al., 1998; Shackleton, 1967), whereas the magnesium content of their shells increases exponentially with increasing temperatures (e.g., Lea et al., 1999). Thus, both SSTs and surface $\delta^{18}O_{sw}$ can be determined by measuring $\delta^{18}O_{shell}$ and Mg/Ca ratios in tandem from fossil planktic foraminifers (e.g. Anand et al., 2003; Anand et al., 2008; Dahl and Oppo, 2006; Elderfield and Ganssen, 2000; Flower et al., 2004).

The PETM was first characterized using foraminifer stable isotope records constructed for the Site 690 section (Kennett and Stott, 1991), so this stratigraphic section has played a central role in shaping our perception of the PETM. Yet a complementary SST record based on planktic foraminifer Mg/Ca ratios has hitherto been lacking for this iconic PETM section. We address this shortcoming by reporting two parallel planktic foraminifer Mg/Ca ratio records that were independently generated using different analytical techniques, which show similar values and trends through the Site 690 PETM section. Added incentive for targeting the Site 690 section is that it represents one of only a handful of PETM records from the circum-Antarctic region (Fig. 1), and as such is geographically well positioned for monitoring changes in the poleward flux of atmospheric moisture during the PETM. This is the case because Rayleigh distillation renders the $\delta^{18}O$ of atmospheric water vapor (and precipitation) extremely ^{18}O-depleted relative to that of the surface ocean (Craig and Gordon, 1965). Thus, a perturbation to the global hydrological cycle resulting in enhanced poleward transport of atmospheric moisture should be signaled by a reduction in surface $\delta^{18}O_{sw}$ (and SSS) at Site 690. It is for this reason that the prominent minimum seen in the published (Kennett and Stott, 1991) planktic foraminifer $\delta^{18}O_{shell}$ record about midway through the CIE interval in the Site 690 PETM section is of particular interest to this study.

2. Material and Methods

2.1. Study site, materials, and chronostratigraphic framework

Site 690 was drilled ~400 km offshore of Antarctica (65°09'S, 01°12'E) along the southwestern flank of Maud Rise in the Weddell Sea at a water depth of 2,940 meters (Barker and Kennett, 1988). Benthic foraminifer assemblages indicate a lower bathyal (~1900 m) paleo-water depth during the late Paleocene (Thomas, 1990). This relatively shallow bathymetric setting is thought to have helped minimize carbonate dissolution at Site 690; nevertheless, sedimentary calcite content decreases at the base of the section (Farley and Eltgroth, 2003; Röhl et al., 2000). The Site 690 PETM section has been studied extensively, and is well-constrained by microfossil biostratigraphies (Bralower, 2002; Kelly, 2002) and foraminifer stable isotope ($\delta^{13}C$, $\delta^{18}O$) records (Kennett and Stott, 1991; Thomas et al., 2002).

The highly-resolved bulk-carbonate $\delta^{13}C$ ($\delta^{13}C_{bulk}$) stratigraphy published for the Site 690 section (Bains et al., 1999), as well as complementary foraminifer stable isotope records (Kennett and Stott, 1991; Thomas et al., 2002), served to guide sample selection. Accordingly, the study section (~171.12 to 169.04 meters below seafloor, mbsf) comprises a stratigraphic series of twenty-three core samples spanning the pre-CIE to CIE transition and extending upwards into the lower part of the CIE recovery of the Site 690 PETM section (see Table S1). The bulk-sediment samples were disaggregated using a pH-buffered sodium hexametaphosphate hydrogen peroxide (30%) solution, wet sieved (>63 µm), rinsed with distilled water, and oven-dried (30°C) overnight. Whenever possible, roughly 20 shells of the planktic foraminifer species *Acarinina soldadoensis* were handpicked from narrow size ranges (250 – 300 µm or 300 – 355 µm) of each core sample. The stable isotope signature of *A. soldadoensis* indicates that this species harbored photosymbionts and inhabited the euphotic zone of the oceanic mixed layer (Quillévéré et al., 2001), so its depth ecology is well suited for reconstructing surface-ocean conditions.

The Site 690 PETM stratigraphy has been calibrated against an astronomically tuned age model, with the resulting ages being reported relative to the CIE onset in the $\delta^{13}C_{bulk}$ record (Röhl et al., 2007). However, a recent study (Hupp et al., 2019) has shown that size-dependent sediment mixing has resulted in a ~14-cm stratigraphic offset between the core depths where the CIE onset is first registered by planktic foraminifer shells (*Acarinina* spp., >250 µm) and bulk-carbonate samples (Fig. 2A). Based on the sedimentation rates reported by Röhl et al. (2007), we estimate that this stratigraphic offset equates to a temporal discrepancy of ~7.31 ka. Our $\delta^{18}O$ and Mg/Ca ratio records were compiled from the same planktic foraminifer genus (*Acarinina*) and size fraction (>250 µm) used to construct the high-resolution, planktic foraminifer $\delta^{13}C$ record for the Site 690 PETM section (Thomas et al., 2002). As a result, we used the core depth (170.78 meters) of the CIE onset in the *Acarinina* spp. $\delta^{13}C$ record

($\delta^{13}C_{acarininid}$) as our chronostratigraphic reference point in order to maintain internal consistency. An added constraint on sample selection is that the response of planktic foraminifers to PETM conditions entailed a high degree of taxonomic turnover at Site 690, with *A. soldadoensis* temporarily disappearing from the overlying CIE recovery interval (Kelly et al., 2005).

In short, the geochemical records herein reported begin ~34 cm below the stratigraphic level of the CIE onset in the $\delta^{13}C_{acarininid}$ record, and extend up-section across the pre-CIE to CIE transition through the interval over which the prominent minimum in the planktic foraminifer $\delta^{18}O_{shell}$ record occurs in the Site 690 PETM section (Fig. 2). We assigned the CIE onset in the $\delta^{13}C_{acarininid}$ record an age of 0.0 ka, and adjusted the previously reported ages for our samples accordingly with all sample ages being reported relative (± ka) to the CIE onset in the $\delta^{13}C_{acarininid}$ record. Our revised age model indicates that the study section initiates at -17.36 ka and ends at +101.85 ka relative to the CIE onset in the $\delta^{13}C_{acarininid}$ record (Table S1).

2.2. Foraminifer preservation

All planktic foraminifer shells from the PETM section of Site 690 feature a 'frosty' (opaque) hue when observed under reflected light, with acarininid shells possessing thickened blade-like structures (termed muricae, Blow, 1979) protruding from their surfaces. These are the telltale signs of post-depositional diagenesis (Kozdon et al., 2013; Pearson et al., 2001; Sexton et al., 2006), which is problematic for conventional planktic foraminifer $\delta^{18}O_{shell}$ analyses requiring acid-digestion of entire shells. In addition, post-depositional diagenesis tends to smooth long-term paleoclimate trends in planktic foraminifer $\delta^{18}O_{shell}$ records (Killingley, 1983), and has demonstrably attenuated the amplitude of the negative $\delta^{18}O_{shell}$ excursion signaling PETM conditions at some sites (Kozdon et al., 2013). In this study, we attempt to minimize the unwanted effects of diagenetic overprinting by performing *in situ* analyses of better-preserved domains within individual foraminifer shells. Specifically, previous study has shown that the basal areas of muricae contain no mural pores, making these minute domains less susceptible to diagenesis and ideal targets for *in situ* measurements of both $\delta^{18}O$ and Mg/Ca ratios (Kozdon et al., 2013). This approach allows for the selection of better-preserved domains as well as the acquisition of both proxies within the same homologous domain of each shell. Conventional 'solution-phase' measurements of Mg/Ca ratios were also performed in parallel for comparison with *in situ* measurements of Mg/Ca ratios.

2.3. *In situ* $\delta^{18}O$ and Mg/Ca measurements

Detailed descriptions of $\delta^{18}O$ measurements in foraminifer shells by secondary ion mass spectrometry (SIMS) are published elsewhere (Kozdon et al., 2009; Kozdon et al., 2011). In

short, acarininid shells were cast in epoxy, ground to midsection and imaged by SEM to identify suitable domains for analysis. *In situ* $\delta^{18}O$ data were acquired in the WiscSIMS Laboratory at the Department of Geoscience, UW-Madison, using a CAMECA IMS-1280 large radius multicollector SIMS (Kita et al., 2009; Valley and Kita, 2009) with analytical conditions similar to those reported by Kozdon et al. (2011). Depending on the size of the target, samples were analyzed with a 10 µm or 3 µm primary beam (Table S2). Four consecutive measurements of UWC-3 calcite standard ($\delta^{18}O$ = 12.40‰ Vienna standard mean ocean water; VSMOW; Kozdon et al., 2009) were performed before and after every set of typically 10 sample analyses. The average analytical precision (reproducibility) for 10 µm-beam conditions was 0.3‰ (± 2 SD, spot-to-spot), and ±0.7‰ for analysis performed with a 3 µm primary beam. Every polished acarininid shell featured several suitable domains for *in situ* measurements. We found that intrashell $\delta^{18}O$ variation of these domains is typically within analytical error, thus only 1-2 *in situ* SIMS $\delta^{18}O$ measurements were performed in each acarininid shell. After SIMS $\delta^{18}O$ measurements, the appearance of each analysis pit was assessed by SEM imaging. We consider $\delta^{18}O$ data from 'irregular' pits (Cavosie et al., 2005) overlapping epoxy resin, cracks, and cavities as being possibly compromised, and values from these measurements were excluded from the data set.

In situ Mg/Ca ratios were acquired from ~3-µm diameter spots within the muricae bases of the acarininid shells using a CAMECA SX-51 electron microprobe at the UW-Madison Department of Geoscience with analytical conditions similar to those previously reported (Kozdon et al., 2013). Whenever possible, Mg/Ca analyses were made adjacent to the SIMS analysis pits or in comparable domains within the same chamber. Only EPMA analytical totals of 98.5 – 100.5 wt.% were considered acceptable (Table S3). As previously reported by Nürnberg (1995), Mg/Ca measurements in planktic foraminifer shells by EPMA exhibit a substantial degree of intrashell variation due to various processes affecting biocalcification (e.g., Bentov and Erez, 2006; Eggins et al., 2003). Thus, whenever possible, multiple Mg/Ca measurements were made in each acarininid shell and used to calculate the average value of each specimen.

For comparative purposes, a parallel whole-shell planktic foraminifer Mg/Ca record was constructed independently. From each sample, 15-25 shells of *A. soldadoensis* (250-300 µm size fraction) were crushed and cleaned with a reductive-oxidative treatment (Boyle and Keigwin, 1985 as revised by Martin and Lea, 2002) prior to being dissolved in 0.075 N HNO₃. The Mg/Ca ratios were measured using a Finnegan Element XR inductively coupled plasma mass spectrometer (ICP-MS) housed at the University of California Santa Cruz and following the methods of Brown et al. (2011). Based on replicate measurements of an in-house carbonate standard, external precision on calcite Mg/Ca ratios is 2% (RSD).

2.4. Calculation of Mg/Ca temperature anomalies

Pre-CIE baseline conditions were determined by EPMA measurements of 19 shells from four core samples ranging from 170.81 to 171.12 mbsf (-1.53 to -17.36 ka relative to the CIE onset), with an average Mg/Ca ratio of 2.63 mmol/mol (Table S4). The PETM is associated with a significant (~0.3 pH units) drop in ocean pH (e.g. Babila et al., 2018; Gutjahr et al., 2017; Penman et al., 2014), which is estimated to increase the Mg/Ca ratios of foraminifer shells by about 15% (Evans et al., 2016b). The δ^{11}B and B/Ca records by Penman et al. (2014) indicate an abrupt and sustained acidification of the upper ocean coincident with the onset of the PETM. Therefore, all Mg/Ca ratios above the CIE onset (1.57 ka to 101.85 ka after CIE onset, Table S1) were adjusted by 15% to account for the effect ocean acidification on foraminifer Mg/Ca, whereas pre-CIE Mg/Ca ratios remained uncorrected.

The temperature dependence of foraminifer Mg/Ca to temperature is described by the general equation (e.g., Anand et al., 2003; Lea et al., 1999):

(1)
$$Mg/Ca_{shell} = B \times \exp^{A \times T}$$

where Mg/Ca is in mmol/mol, T is the calcification temperature in °C, A is the exponential constant for temperature sensitivity, and B is the pre-exponential constant. A range of values for B and A has been published based on shells from plankton tows, sediment traps, core tops, or culture experiments (e.g., Anand et al., 2003; Elderfield and Ganssen, 2000; Gray et al., 2018; Lea et al., 1999; Rosenthal et al., 1997). For the calculation of relative temperature changes with respect to pre-CIE conditions, the pre-exponential constant B is not required. Accordingly, Mg/Ca temperature anomalies were calculated using the equation of Zachos el. (2003):

(2)
$$\Delta T = \frac{1}{A}\ln\left[\left(\frac{C}{100}\right) + 1\right]$$

where ΔT is the relative change in temperature (°C), and C is the percentage change in Mg/Ca with respect to the mean pre-CIE baseline Mg/Ca value of 2.63 mmol/mol.

Use of planktic foraminifer Mg/Ca ratios to calculate SSTs must take into account the Mg/Ca ratio of past seawater (Mg/Ca$_{sw}$). Coupled clumped-isotope and Mg/Ca ratio measurements of foraminifer shells from a set of globally distributed sites suggest that the Mg/Ca ratio of early Eocene seawater was ~2 mol/mol, ~40% of modern (Evans et al., 2018). Comparably lower values of early Eocene Mg/Ca$_{sw}$ were determined by analyses of calcite veins that had precipitated from seawater-derived fluids in ocean ridge flank basalts (Coggon et al., 2010). In addition, the response of foraminifer Mg/Ca to lower Mg/Ca$_{sw}$ is nonlinear (Evans et al., 2015a; Evans et al., 2016a; Segev and Erez, 2006), and the exponential constant A for lower Mg/Ca$_{sw}$ needs to be determined. As the planktic foraminifer species used in this study is extinct, we used the adjustment for lower Mg/Ca$_{sw}$ reported by Evans et al. (2016a),

which is based on the response of cultured specimens of the modern planktic foraminifer species *Globigerinoides ruber* to variations in Mg/Ca_{sw}:

(3) $$A = -0.0029 \times Mg/Ca_{sw}^2 + 0.032 \times Mg/Ca_{sw}$$

With an early Eocene Mg/Ca_{sw} value of 2.0 mol/mol, the exponential constant A calculated by equation (3) is 0.056. This value is used in equation (2) to calculate Mg/Ca temperature anomalies.

2.5. Calculation of $\delta^{18}O$-temperature, $\delta^{18}O_{sw}$ composition, and salinity anomalies

For the calculation of $\delta^{18}O$-based temperature anomalies, pre-CIE baseline conditions were determined by averaging *in situ* $\delta^{18}O$ analyses in 13 shells from four core samples ranging from 170.81 to 171.12 mbsf (-1.53 to -17.36 ka relative to the CIE onset) with an average $\delta^{18}O$ value of -2.21‰ (Table S3). Similar to Mg/Ca, planktic foraminifer $\delta^{18}O$ values are sensitive to changes in ocean pH. Therefore, $\delta^{18}O_{SIMS}$ values from shells sampled within the CIE interval (+1.57 ka to +101.85 ka after CIE onset, Table S3) were adjusted by 0.27‰ (Uchikawa and Zeebe, 2010) to account for the abrupt and sustained drop of 0.3 pH units after the CIE onset (sensitivity of -0.89‰/pH unit). Pre-CIE $\delta^{18}O$ values remained unadjusted. The relationship between ocean pH and planktic foraminifer $\delta^{18}O$ has been robustly characterized for only two modern species, and their sensitivities vary significantly (-0.89‰/pH unit and -2.51‰/pH unit, Spero et al., 1997; Uchikawa and Zeebe, 2010). We therefore performed additional calculations using the higher sensitivity of -2.51‰/pH unit and show these results in the Supplementary Material (Fig. S5, SOM). The $\delta^{18}O$ temperature anomaly relative to the pre-CIE baseline was calculated using a $\Delta\delta^{18}O_{calcite}/\Delta T$ relation of -0.213‰/°C (e.g., Zachos et al., 2003).

Differences between the $\delta^{18}O_{SIMS}$ and Mg/Ca-based SST anomaly records suggest local changes in surface $\delta^{18}O_{sw}$ driven by secular variation in the precipitation-evaporation balance at Site 690. We therefore used the $\Delta\delta^{18}O_{shell}/\Delta T$ relation (-0.213‰/°C) to convert these differences to expected changes in surface $\delta^{18}O_{sw}$ composition. For example, if the SST anomalies calculated independently from Mg/Ca and $\delta^{18}O$ differ by 1°C, past surface $\delta^{18}O_{sw}$ needs to be adjusted by 0.213‰ so that both temperature anomalies feature the same values with respect to pre-CIE baseline conditions. The adjustment to $\delta^{18}O_{sw}$ (0.213‰) used to reconcile the difference between $\delta^{18}O_{SIMS}$ and Mg/Ca-based SST anomaly records is then converted to change in sea surface salinity (SSS). However, the $\Delta\delta^{18}O_{sw}/D_{salinity}$ relation is not well constrained for early Eocene high latitude oceans, and varies from 0.25‰/salinity unit to 0.50‰/salinity unit (Zachos et al., 2003). Depending on the $\Delta\delta^{18}O_{sw}/D_{salinity}$ relation, the adjustment of 0.213‰ to $\delta^{18}O_{sw}$ corresponds to a change in SSS between ~0.45 and ~0.9 psu. We therefore use both of the aforementioned $\Delta\delta^{18}O_{sw}/D_{salinity}$ relations to delimit SSS variation expressed in our $\delta^{18}O_{sw}$ record.

Planktic foraminifer Mg/Ca ratios are also sensitive to salinity, showing a ~3% to 5% decrease in Mg/Ca with for each unit decrease in salinity (e.g., Hönisch et al., 2013). Thus, an adjustment for salinity should be considered as uncorrected Mg/Ca values may cause a significant overestimation of the salinity shift. We caution, however, that such a salinity correction involves a degree of circular reasoning since salinity variation was initially based on paired $\delta^{18}O$:Mg/Ca analyses. With this caveat in mind, we adjusted our planktic foraminifer Mg/Ca ratios to more fully appreciate how changes in salinity might influence our Mg/Ca-based SST and $\delta^{18}O_{sw}$ reconstructions. This 'sensitivity test' was carried out using an empirically-derived relation (ΔMg/Ca = 4% per salinity unit) for salinity effect (Hönisch et al., 2013) and the average salinities (i.e. mean of the 'salinity field' defined by the $\Delta\delta^{18}O_{sw}$/$D_{salinity}$ relation ranging from 0.25‰/salinity unit to 0.50‰/salinity unit) that were initially computed for each core sample without any salinity correction to iteratively adjust our measured Mg/Ca ratios. The resulting 'salinity-corrected' Mg/Ca ratios were then used to recalculate the Mg/Ca-temperature anomaly record. The differences between the $\delta^{18}O_{SIMS}$ and salinity-corrected Mg/Ca SST anomalies were then used to recalculate $\delta^{18}O_{sw}$ and SSS anomalies (Table S3). The salinity correction for Mg/Ca reduces the amplitude of the SSS anomaly by about 40%.

3. Results

Given the uncertainties surrounding both the $\delta^{18}O$ and Mg/Ca ratio records, we opted not to report absolute values for the various environmental parameters (SST, $\delta^{18}O_{sw}$, and SSS), and instead describe environmental change during the PETM as 'anomalies' *relative* to the pre-CIE baseline conditions. With this being said, we note that the $\delta^{18}O_{SIMS}$ and published acarininid $\delta^{18}O_{shell}$ records (Kennett and Stott, 1991) delineate grossly similar trends (Fig. 2B), but the $\delta^{18}O_{SIMS}$ values are, on average, ~1‰ lower than corresponding $\delta^{18}O_{shell}$ values. Owing to the frosty appearance of the acarininid shells, we attribute this systematic offset to measurement of ^{18}O-enriched diagenetic calcite by conventional whole-shell gas-source mass spectrometry, although inter-instrument $\delta^{18}O$ differences cannot be ruled out (e.g., Wycech et al., 2018). The $\delta^{18}O_{SIMS}$ and $\delta^{18}O_{shell}$ records show quasi-simultaneous shifts toward lower values just above the CIE onset, and feature minima ($\delta^{18}O_{SIMS}$: -3.8‰, $\delta^{18}O_{shell}$: -2.2‰) ~50 ka after the CIE onset. This same interval also exhibits the largest $\delta^{18}O_{SIMS-shell}$ offset (approaching 1.5‰) between these two analytical approaches (Fig. 2B). The total amplitude of the $\delta^{18}O$ decrease is ~2‰ and ~2.5‰ in the $\delta^{18}O_{shell}$ and $\delta^{18}O_{SIMS}$ records, respectively. Starting at about +60 ka after the CIE onset, $\delta^{18}O$ values in both records steadily increase back toward pre-CIE values before ending near the base of the CIE recovery interval (Fig. 2B).

The two, parallel Mg/Ca records show similar values and trends (Fig. 2C), thereby precluding an inter-instrument or method-related bias between the *in situ* EPMA and

conventional ICP-MS measurements. Both of the Mg/Ca records feature an abrupt, but short-lived, ~2 mmol/mol increase immediately above the level of the CIE onset that is not accompanied by a decrease in the $\delta^{18}O_{SIMS}$ and $\delta^{18}O_{shell}$ records (Figs. 2B, C). The stratigraphic expression of this transient increase differs slightly in the two Mg/Ca records with the conventional ICP-MS record featuring a 'double peak' that is less clearly defined and somewhat concatenated in the EPMA-derived record (Fig. 2C). This minor discrepancy notwithstanding, Mg/Ca ratios in both records subsequently decline to values (~2.5 mmol/mol) approaching the pre-CIE baseline, and remain relatively invariant over the very interval in which the minima in the $\delta^{18}O_{shell}$ and $\delta^{18}O_{SIMS}$ records occur (Figs. 2B, C).

4. Discussion

4.1. Local Sea-Surface Temperature Anomaly at Site 690

The significance of the differences between the $\delta^{18}O_{SIMS}$ and Mg/Ca records becomes more evident when the two proxies are used to generate separate SST-anomaly records (Fig. 3A). The $\delta^{18}O$ composition of foraminifer shells is a function of temperature and ambient seawater $\delta^{18}O_{sw}$, with rates of precipitation/evaporation (i.e. salinity effect) and changes in continental ice volume being the primary controls on $\delta^{18}O_{sw}$ (e.g. Emiliani, 1955; Shackleton, 1974). The latter factor, ice volume effect, is discounted owing to the absence of large continental ice sheets during the time period encompassing the PETM (Francis, 1988). Thus, after adjusting measured $\delta^{18}O$ values from within the CIE interval by 0.27‰ to account for a drop of ~0.3 units in ocean pH (Gutjahr et al., 2017; Penman et al., 2014; Uchikawa and Zeebe, 2010), the $\delta^{18}O$-based temperature anomalies were calculated using the $\Delta\delta^{18}O_{shell}/\Delta T$ relation of -0.213°C and assuming that local surface $\delta^{18}O_{sw}$ remained constant (Shackleton and Kennett, 1975; Zachos et al., 2001). Likewise, the use of Mg/Ca ratios as an independent proxy for SST is complicated by secular variation in the Mg/Ca ratio of seawater. Most reconstructions indicate that the Mg/Ca ratio of seawater has increased over the Cenozoic, and early Eocene values for Mg/Ca_{sw} were possibly as low as 2.0 mol/mol (Coggon et al., 2010; Evans et al., 2018). The response of foraminifer Mg/Ca to lower seawater Mg/Ca is nonlinear, and the pre-exponential constant of the Mg/Ca temperature equation needs to be adjusted accordingly (Evans et al., 2016a). In addition, the pH drop of 0.3 units could have resulted in a 15% increase in foraminifer Mg/Ca (Evans et al., 2015b). Therefore, the Mg/Ca temperature anomaly record (Fig. 3A) is adjusted for lower Eocene seawater Mg/Ca and a ~0.3 drop in ocean pH (Table S4). An additional adjustment for the effects of salinity on foraminifer Mg/Ca ratios was also applied (see Section 2.5. for more details).

Major discrepancies in the timing and amplitude of *peak* PETM warming are evident between the two SST anomaly records even after adjusting both the $\delta^{18}O$ and Mg/Ca records for the effects of various non-thermal factors (Fig. 3A). Peak warming in the $\delta^{18}O_{SIMS}$ record

is signaled by an apparent ~9°C anomaly at +50 ka after the CIE onset, whereas peak warming in the *in situ* Mg/Ca record is signaled by an abrupt ~4°C increase in SSTs just after the CIE onset at +3.13 ka. The curious 'double peak' of the SST anomaly delineated by both of our Mg/Ca records could be construed as indicating that the earliest stages of the PETM entailed two pulses of ~4°C warming, one just after the CIE onset (~+3 ka) and a second at about +8 ka (Fig. 3A). However, a similar double peak in warming has not been seen in other pelagic PETM sections; hence, we cannot rule out the possibility that this curious feature of our Mg/Ca records may be an artifact of sediment mixing processes at Site 690 (e.g., Hupp et al., 2019; Kirtland Turner et al., 2017; Thomas et al., 2002). After this brief increase in SSTs, Mg/Ca-based temperatures return to near pre-CIE values at +11.58 ka, followed by a slight increase (~2-3°C above pre-CIE condition) over the interval (+30 to +80 ka) in which apparent peak warming is signaled by the $\delta^{18}O_{SIMS}$ minimum (Fig. 3A).

The amplitude of the local SST anomaly (4-5°C) registered by the Mg/Ca record is only about half of that inferred (~9°C) from the published Site 690 $\delta^{18}O_{shell}$ record, and falls at the lower end of estimates (~5-7°C) obtained from an organic-based SST proxy (TEX_{86}) record generated for another PETM section in the Southern Ocean (Sluijs et al., 2011). Instead, our estimate of 4-5°C warming is more comparable in scale to SST anomalies reported for PETM sections from tropical (Aze et al., 2014; Zachos et al., 2003) and Arctic (Sluijs et al., 2006) regions, and is consonant with the estimated global mean surface temperature anomaly (4-5 °C) for the PETM (Jones et al., 2013). An interesting corollary to our estimate for peak warming (~4-5°C) at Site 690 is that it contradicts is the notion of "polar amplification" in the absence of ice-albedo effects during the PETM (e.g., Sluijs et al., 2006).

The absence of polar amplification in our SST anomaly reconstruction could be an artifact stemming from the selective dissolution of Mg-rich domains within the planktic foraminifer shells (e.g., Dekens et al., 2002; Rosenthal et al., 2000), which would attenuate the true amplitude of the local SST anomaly expressed in both of the Mg/Ca records. The drop in sedimentary calcite content associated with the CIE onset at Site 690 is a common feature of pelagic PETM sections (e.g., Bralower et al., 2014; Colosimo et al., 2006; Thomas et al., 1999) and reflects a pulse of intensified carbonate dissolution fueled by a CO_2-induced drop in ocean pH (Dickens et al., 1997; Penman et al., 2014; Zachos et al., 2005). Thus, a possible role for selective dissolution is consistent with the decrease in sedimentary calcite content and increase in planktic foraminifer shell fragmentation, as documented by Kelly et al. (2005), over the same interval featuring the Mg/Ca-based SST anomaly in the Site 690 PETM record. It is also possible that carbonate dissolution at Site 690 was more severe, and that the basal stratigraphy of this PETM section may be incomplete as recently argued by others (Ajayi et al., 2020; Zhang et al., 2020). If the base of the CIE interval is truncated by hiatus, then the ~4-5°C of warming may represent a minimum.

This being said, we note that signs of intra-shell dissolution and etching were not observed in the many shells cross-sectioned for *in situ* analyses, although we acknowledge that, while the analyzed domains within the acarininid shells are better preserved than other parts of the same shells, they are likely not pristine. To a first approximation, secular variation in our Mg/Ca-based SST anomaly record appears to track model (LOSCAR) simulations for carbon input during the PETM (Zeebe et al., 2009). Specifically, the transient (<10 kyrs) peak in SSTs reflects enhanced greenhouse radiative forcing caused by a large carbon-input event at the CIE onset followed by a more prolonged period (~50 kyrs) of slightly cooler but still warm SSTs sustained by continued carbon release at slower rates over the main part of the CIE. Thus, the stratigraphic profile of our Mg/Ca-based SST anomaly curve may reflect secular variation in radiative forcing at this climatically sensitive location driven by two phases of carbon input that differ in their timing, duration, and emission rate during the PETM.

4.2. Changes in surface ocean $\delta^{18}O_{sw}$ and SSS at Site 690

The most parsimonious explanation for the disparities seen between the $\delta^{18}O_{SIMS}$ and Mg/Ca SST anomaly records is local changes in surface $\delta^{18}O_{sw}$ driven by secular variation in the precipitation-evaporation balance at Site 690. To explore the implications of this alternative interpretation, we used the $\Delta\delta^{18}O_{shell}/\Delta T$ relation of 0.213‰/°C to convert the differences between corresponding $\delta^{18}O_{SIMS}$ and Mg/Ca SSTs to expected changes in surface $\delta^{18}O_{sw}$ (Zachos et al., 2003). The resulting record reveals that a brief excursion to higher surface $\delta^{18}O_{sw}$ values coincided with peak PETM warming just after the CIE onset in the $\delta^{13}C_{acarininid}$ record (Fig. 3B). However, the most salient feature is a prominent decrease where surface $\delta^{18}O_{sw}$ values drop as low as -1.4‰ relative to the pre-CIE baseline over the interval (+30 to +80 ka) in which the $\delta^{18}O_{SIMS}$ minimum occurs. This finding differs from the long-held view that the $\delta^{18}O_{shell}$ minimum at +50 ka signals peak PETM warming (e.g., Kennett and Stott, 1991), and indicates that this $\delta^{18}O_{shell}$ minimum actually reflects a significant decrease in surface $\delta^{18}O_{sw}$ at Site 690. Surface $\delta^{18}O_{sw}$ values subsequently increase to values approaching the pre-CIE baseline at about +80 ka (Fig. 3B).

Conversion of the surface $\delta^{18}O_{sw}$ values to SSS anomalies indicates that *peak* PETM warming was accompanied by a brief increase of ~2 ppt in SSS at Site 690 (Fig. 3C). The width of the 'salinity anomaly field' is a function of the selected $\Delta\delta^{18}O_{sw}/D_{salinity}$ relation, which varies from 0.25‰/salinity unit to 0.50‰/salinity unit (Zachos et al., 2003). On the basis of our paired $\delta^{18}O_{SIMS}$:Mg/Ca records, we conclude that peak PETM warming and an increase in SSS, reflecting a transient shift to warmer, more arid conditions at Site 690, was tightly coupled to initial carbon input. The ensuing $\delta^{18}O_{sw}$ minimum equates to a reduction in SSS beginning at about +30 ka with the lowest values (~2.9 to 5.8 ppt lower than pre-CIE baseline) occurring at about +50 ka (Fig. 3C). This local negative SSS anomaly signals a transient increase in mean

annual precipitation sustained by an increase in the poleward flux of atmospheric moisture at Site 690. Computed SSS anomalies subsequently increase to values approaching the pre-CIE baseline at about +80 ka (Fig. 3C).

4.3. Implications for carbon cycling and continental weathering during the PETM

Such extreme fluctuations in the meridional balance between precipitation and evaporation would have influenced carbon cycling over the course of the PETM (John et al., 2008). If the initial shift to warmer, drier conditions occurred over geographically expansive tracts of the mid- and high-latitudes then the oxidation of sedimentary organic matter may have contributed to the CO_2 flux emitted during the early stages of the PETM (e.g., Kurtz et al., 2003; Panchuk et al., 2008). The ensuing reversal to slightly cooler SSTs, but substantially lower SSSs, is the most robust feature delineated by our paired $\delta^{18}O_{SIMS}$:Mg/Ca record, and culminates in a negative SSS anomaly that is ~4 ppt lower than the mean pre-CIE value (Fig. 3C). This significant downturn in SSS signals a major change in the meridional balance between precipitation and evaporation, which in turn increased the poleward transport of atmospheric moisture and mean annual precipitation at Site 690. This particular result is consonant with General Circulation Models predicting greater poleward migration of storm tracks under a warmer climate regime (Caballero and Langen, 2005). Such an extreme turnabout in hydrological regime would have altered spatial patterns of continental erosion/sedimentation and likely intensified chemical weathering of landmasses (Carmichael et al., 2017; 2018). Such a supposition is supported by the marked increases in siliciclastic sedimentation at nearshore, shallow marine sites during the PETM (John et al., 2008; Nicolo et al., 2010), and by a concomitant change in clay mineralogy to predominantly kaolinite in some geological sections (Bolle and Adatte, 2001; Clechenko et al., 2007; Gibson et al., 2000). Although the syngenecity of kaolinitization and PETM conditions has been questioned (John et al., 2012; Thiry, 2000), and even attributed to the redeposition of a rapidly weathered impact ejecta dust blanket (Kent et al., 2003), a similar increase in kaolinite amongst detrital clay assemblages in the Site 690 section has been ascribed to increased continental weathering and freshwater input driven by a transient increase in atmospheric heat transport toward the poles (Kelly et al., 2005; Robert and Kennett, 1994). Here, we note that the latter interpretation (Robert and Kennett, 1994) is consistent with the prominent negative SSS anomaly recorded over the CIE interval (+30 ka to +80 ka) at Site 690. The apparent lag in local hydrologic response to warming might be related to orbital effects (Kiehl et al., 2018).

5. Conclusions

Paired $\delta^{18}O$:Mg/Ca analyses, acquired *in situ* from micrometer-scale domains within shells of the planktic foraminifer, *A. soldadoensis,* indicate that peak PETM warming was coupled to an increase in SSS at ODP Site 690 (Weddell Sea). This initial shift to hotter, more arid

conditions was tightly coupled to the initial release of massive quantities of carbon to the atmosphere. The local SST anomaly of ~4ºC reflecting peak PETM warming at Site 690 may represent a minimum owing to the possibility that the base of the PETM section is truncated by a hiatus. A prominent ~4 ppt decrease in SSS, back-calculated from paired $\delta^{18}O$:Mg/Ca measurements, is observed ~50 ka after peak PETM warming. This negative SSS ($\delta^{18}O_{sw}$) anomaly coincides with a minimum in the Site 690 planktic foraminifer $\delta^{18}O$ record that has previously been cited as evidence for polar amplification of PETM warmth in the absence of ice-albedo effects. Thus, our revised interpretation posits that this $\delta^{18}O$ minimum actually signals a decrease in surface-ocean $\delta^{18}O_{sw}$ fostered by a transient increase in mean annual precipitation in the Weddell Sea region, thereby corroborating the view that the poleward flux of atmospheric moisture temporarily increased during a distinctive stage of the PETM.

Such data-based reconstructions of the response of Earth's hydrological cycle to greenhouse gas forcing are vital to understanding how atmospheric moisture and latent heat were redistributed across the planet during past episodes of global warming. This study confirms that Earth's hydrological cycle was profoundly perturbed by massive carbon input during the PETM, and the highly resolved chronostratigraphy of the Site 690 section provides temporal constraints on secular variation in the poleward flux of atmospheric moisture and latent heat. The surface $\delta^{18}O_{sw}$ (and SSS) record herein reconstructed for the Site 690 PETM section improves geographic coverage in the climatically sensitive circum-Antarctic region, which should prove useful for testing outcomes of computational models designed to simulate PETM climatic conditions.

Acknowledgements

Data Availability Statement

Data tables of *in situ* $\delta^{18}O$ and Mg/Ca analyses are available from the PANGAEA domain repository (https://doi.org/10.1594/PANGAEA.914650, https://doi.org/10.1594/PANGAEA.914651).

References

Ajayi, S., L. R. Kump, A. Ridgwell, S. Kirtland Turner, C. C. Hay, and T. J. Bralower (2020), Evaluation of Paleocene-Eocene Thermal Maximum Carbon Isotope Record Completeness—An Illustration of the Potential of Dynamic Time Warping in Aligning Paleo-Proxy Records, *Geochemistry, Geophysics, Geosystems*, *21*(3), e2019GC008620, doi:10.1029/2019gc008620.

Anand, P., H. Elderfield, and M. H. Conte (2003), Calibration of Mg/Ca thermometry in planktonic foraminifera from a sediment trap time series, *Paleoceanography*, *18*(2), 1050, doi:10.1029/2002pa000846.

Anand, P., D. Kroon, A. D. Singh, R. S. Ganeshram, G. Ganssen, and H. Elderfield (2008), Coupled sea surface temperature–seawater $\delta^{18}O$ reconstructions in the Arabian Sea at the millennial scale for the last 35 ka, *Paleoceanography*, *23*(4), PA4207, doi:10.1029/2007pa001564.

Aze, T., et al. (2014), Extreme warming of tropical waters during the Paleocene–Eocene Thermal Maximum, *Geology*, doi:10.1130/g35637.1.

Babila, T. L., Y. Rosenthal, J. D. Wright, and K. G. Miller (2016), A continental shelf perspective of ocean acidification and temperature evolution during the Paleocene-Eocene Thermal Maximum, *Geology*, *44*(4), 275-278, doi:10.1130/g37522.1.

Babila, T. L., D. E. Penman, B. Hönisch, D. C. Kelly, T. J. Bralower, Y. Rosenthal, and J. C. Zachos (2018), Capturing the global signature of surface ocean acidification during the Palaeocene–Eocene Thermal Maximum, *Philosophical Transactions of the Royal Society A: Mathematical, Physical and Engineering Sciences*, *376*(2130), 20170072.

Bains, S., R. M. Corfield, and R. D. Norris (1999), Mechanisms of Climate Warming at the End of the Paleocene, *Science*, *285*(5428), 724-727, doi:10.1126/science.285.5428.724.

Barker, P. F., and J. P. Kennett (1988), 6. Site 690. Shipboard Scientific Party., in *Proceedings of the Ocean Drilling Program, Scientific Results Volume 113*, edited by P. F. Barker and J. P. Kennett, College Station, TX.

Bemis, B. E., H. J. Spero, J. Bijma, and D. W. Lea (1998), Reevaluation of the oxygen isotopic composition of planktonic foraminifera: Experimental results and revised paleotemperature equations, *Paleoceanography*, *13*(2), 150-160.

Bentov, S., and J. Erez (2006), Impact of biomineralization processes on the Mg content of foraminiferal shells: A biological perspective, *Geochemistry Geophysics Geosystems*, *7*(1).

Blow, W. H. (1979), *The Cainozoic globigerinida*, E.J. Brill, Leiden.

Bolle, M. P., and T. Adatte (2001), Palaeocene-early Eocene climatic evolution in the Tethyan realm: clay mineral evidence, *Clay Miner.*, *36*(2), 249-261.

Bowen, G. J., D. J. Beerling, P. L. Koch, J. C. Zachos, and T. Quattlebaum (2004), A humid climate state during the Palaeocene/Eocene thermal maximum, *Nature*, *432*(7016), 495-499, doi:http://www.nature.com/nature/journal/v432/n7016/suppinfo/nature03115_S1.html.

Boyle, E. A., and L. D. Keigwin (1985), Comparison of Atlantic and Pacific paleochemical records for the last 215.000 years: Changes in deep ocean circulation and chemical inventories., *Earth Planet. Sci. Lett.*, *76*, 135-150.

Bralower, T. J. (2002), Evidence of surface water oligotrophy during the Paleocene-Eocene thermal maximum: Nannofossil assemblage data from Ocean Drilling Program Site 690, Maud Rise, Weddell Sea, *Paleoceanography*, *17*(2), 1023, doi:10.1029/2001pa000662.

Bralower, T. J., K. J. Meissner, K. Alexander, and D. J. Thomas (2014), The dynamics of global change at the Paleocene-Eocene thermal maximum: A data-model comparison, *Geochemistry, Geophysics, Geosystems*, *15*(10), 3830-3848.

Brown, R. E., L. D. Anderson, E. Thomas, and J. C. Zachos (2011), A core-top calibration of B/Ca in the benthic foraminifers Nuttallides umbonifera and Oridorsalis umbonatus: A proxy for Cenozoic bottom water carbonate saturation, *Earth Planet. Sci. Lett.*, *310*(3–4), 360-368, doi:10.1016/j.epsl.2011.08.023.

Caballero, R., and P. L. Langen (2005), The dynamic range of poleward energy transport in an atmospheric general circulation model, *Geophys. Res. Lett.*, *32*(2), L02705, doi:10.1029/2004gl021581.

Carmichael, M. J., G. N. Inglis, M. P. Badger, B. D. A. Naafs, L. Behrooz, S. Remmelzwaal, F. M. Monteiro, M. Rohrssen, A. Farnsworth, and H. L. Buss (2017), Hydrological and associated biogeochemical consequences of rapid global warming during the Paleocene-Eocene Thermal Maximum, *Global Planet. Change*, *157*, 114-138.

Carmichael, M. J., R. D. Pancost, and D. J. Lunt (2018), Changes in the occurrence of extreme precipitation events at the Paleocene–Eocene thermal maximum, *Earth Planet. Sci. Lett.*, *501*, 24-36.

Cavosie, A. J., J. W. Valley, S. A. Wilde, and E.I.M.F (2005), Magmatic $\delta^{18}O$ in 4400–3900 Ma detrital zircons: A record of the alteration and recycling of crust in the Early Archean, *Earth Planet. Sci. Lett.*, *235*(3–4), 663-681, doi:10.1016/j.epsl.2005.04.028.

Clechenko, E. R., D. C. Kelly, G. J. Harrington, and C. A. Stiles (2007), Terrestrial records of a regional weathering profile at the Paleocene-Eocene boundary in the Williston Basin of North Dakota, *Geological Society of America Bulletin*, *119*(3-4), 428-442, doi:10.1130/b26010.1.

Clementz, M. T., and J. O. Sewall (2011), Latitudinal Gradients in Greenhouse Seawater $\delta^{18}O$: Evidence from Eocene Sirenian Tooth Enamel, *Science*, *332*(6028), 455-458, doi:10.1126/science.1201182.

Coggon, R. M., D. A. H. Teagle, C. E. Smith-Duque, J. C. Alt, and M. J. Cooper (2010), Reconstructing Past Seawater Mg/Ca and Sr/Ca from Mid-Ocean Ridge Flank Calcium Carbonate Veins, *Science*, *327*(5969), 1114-1117, doi:10.1126/science.1182252.

Colosimo, A., T. J. Bralower, and J. C. Zachos (2006), Evidence for lysocline shoaling at the Paleocene/Eocene Thermal Maximum on Shatsky Rise, Northwest Pacific, in *Proceedings of the Ocean Drilling Program, Scientific Results, v. 198*, edited by T. J. Bralower, I. P. Silva and M. J. Malone, pp. 1-36, College Station, TX.

Craig, H., and L. I. Gordon (1965), Deuterium and oxygen 18 variations in the ocean and the marine atmosphere, *Marine Geochemistry*, *3*, 277-374.

Dahl, K. A., and D. W. Oppo (2006), Sea surface temperature pattern reconstructions in the Arabian Sea, *Paleoceanography*, *21*(1), n/a-n/a, doi:10.1029/2005PA001162.

DeConto, R. M., S. Galeotti, M. Pagani, D. Tracy, K. Schaefer, T. Zhang, D. Pollard, and D. J. Beerling (2012), Past extreme warming events linked to massive carbon release from thawing permafrost, *Nature*, *484*(7392), 87-91, doi:http://www.nature.com/nature/journal/v484/n7392/abs/nature10929.html#supplementary-information.

Dekens, P. S., D. W. Lea, D. K. Pak, and H. J. Spero (2002), Core top calibration of Mg/Ca in tropical foraminifera: Refining paleotemperature estimation, *Geochemistry Geophysics Geosystems*, *3(4)*, doi:10.1029/2001GC000200.

Dickens, G. R., J. R. O'Neil, D. K. Rea, and M. Owen (1995), Dissociation of oceanic methane hydrate as a cause of the carbon isotope excursion at the end of the Paleocene., *Paleoceanography*, *10*, 965-971.

Dickens, G. R., M. M. Castillo, and J. C. G. Walker (1997), A blast of gas in the latest Paleocene: Simulating first-order effects of massive dissociation of oceanic methane hydrate, *Geology*, *25*(3), 259-262, doi:10.1130/0091-7613(1997)025<0259:abogit>2.3.co;2.

Egger, H., J. Fenner, C. Heilmann-Clausen, F. Rögl, R. F. Sachsenhofer, and S. B. (2003), Paleoproductivity of the northwestern Tethyan margin (Anthering Section, Austria) across the Paleocene-Eocene transition, in *Climates in the Early Paleogene*, edited by S. L. Wing, P. D. Gingerich, B. Schmitz and E. Thomas, pp. 133-146, Geological Society of America Special Paper, Boulder, Colorado.

Eggins, S. M., P. De Decker, and J. Marshall (2003), Mg/Ca variations in planktonic foraminifera tests: implications for reconstructing paleo-seawater temperature and habitat migration., *Earth Planet. Sci. Lett.*, *212*, 291-306.

Elderfield, H., and G. Ganssen (2000), Past temperature and δ^{18}O of surface ocean waters inferred from foraminiferal Mg/Ca ratios, *Nature*, *405*, 442-445.

Emiliani, C. (1955), Pleistocene temperatures, *Journal of Geology*, *63*, 537-578.

Evans, D., J. Erez, S. Oron, and W. Müller (2015a), Mg/Ca-temperature and seawater-test chemistry relationships in the shallow-dwelling large benthic foraminifera Operculina ammonoides, *Geochim. Cosmochim. Acta*, *148*(0), 325-342, doi:http://dx.doi.org/10.1016/j.gca.2014.09.039.

Evans, D., B. S. Wade, M. Henehan, J. Erez, and W. Müller (2015b), Revisiting carbonate chemistry controls on planktic foraminifera Mg/Ca: implications for sea surface temperature and hydrology shifts over the Paleocene–Eocene Thermal Maximum and Eocene–Oligocene Transition, *Clim. Past Discuss.*, *11*(4), 3143-3185, doi:10.5194/cpd-11-3143-2015.

Evans, D., C. Brierley, M. E. Raymo, J. Erez, and W. Müller (2016a), Planktic foraminifera shell chemistry response to seawater chemistry: Pliocene–Pleistocene seawater Mg/Ca, temperature and sea level change, *Earth Planet. Sci. Lett.*, *438*, 139-148, doi:http://dx.doi.org/10.1016/j.epsl.2016.01.013.

Evans, D., B. S. Wade, M. Henehan, J. Erez, and W. Müller (2016b), Revisiting carbonate chemistry controls on planktic foraminifera Mg /Ca: implications for sea surface temperature and hydrology shifts over the Paleocene–Eocene Thermal Maximum and Eocene–Oligocene transition, *Clim. Past*, *12*(4), 819-835, doi:10.5194/cp-12-819-2016.

Evans, D., et al. (2018), Eocene greenhouse climate revealed by coupled clumped isotope-Mg/Ca thermometry, *Proceedings of the National Academy of Sciences*, *115*(6), 1174-1179, doi:10.1073/pnas.1714744115.

Farley, K. A., and S. F. Eltgroth (2003), An alternative age model for the Paleocene–Eocene thermal maximum using extraterrestrial 3He, *Earth Planet. Sci. Lett.*, *208*(3–4), 135-148, doi:10.1016/s0012-821x(03)00017-7.

Flower, B. P., D. W. Hastings, H. W. Hill, and T. M. Quinn (2004), Phasing of deglacial warming and Laurentide Ice Sheet meltwater in the Gulf of Mexico, *Geology*, *32*(7), 597-600, doi:10.1130/g20604.1.

Foreman, B. Z., P. L. Heller, and M. T. Clementz (2012), Fluvial response to abrupt global warming at the Palaeocene/Eocene boundary, *Nature*, *491*(7422), 92-95, doi:http://www.nature.com/nature/journal/v491/n7422/abs/nature11513.html#supplementary-information.

Francis, J. E. (1988), A 50-Million-Year-Old Fossil Forest from Strathcona Fiord, Ellesmere Island, Arctic Canada: Evidence for a Warm Polar Climate, *Arctic*, *4*(4), 314-318.

Frieling, J., H. Gebhardt, M. Huber, O. A. Adekeye, S. O. Akande, G.-J. Reichart, J. J. Middelburg, S. Schouten, and A. Sluijs (2017), Extreme warmth and heat-stressed

plankton in the tropics during the Paleocene-Eocene Thermal Maximum, *Science advances*, *3*(3), e1600891.

Gibson, T. G., L. M. Bybell, and D. B. Mason (2000), Stratigraphic and climatic implications of clay mineral changes around the Paleocene/Eocene boundary of the northeastern US margin, *Sediment. Geol.*, *134*(1-2), 65-92, doi:10.1016/s0037-0738(00)00014-2.

Gray, W. R., S. Weldeab, D. W. Lea, Y. Rosenthal, N. Gruber, B. Donner, and G. Fischer (2018), The effects of temperature, salinity, and the carbonate system on Mg/Ca in Globigerinoides ruber (white): A global sediment trap calibration, *Earth Planet. Sci. Lett.*, *482*, 607-620.

Gutjahr, M., A. Ridgwell, P. F. Sexton, E. Anagnostou, P. N. Pearson, H. Pälike, R. D. Norris, E. Thomas, and G. L. Foster (2017), Very large release of mostly volcanic carbon during the Palaeocene-Eocene Thermal Maximum, *Nature*, *548*, 573-577.

Handley, L., A. O'Halloran, P. N. Pearson, E. Hawkins, C. J. Nicholas, S. Schouten, I. K. McMillan, and R. D. Pancost (2012), Changes in the hydrological cycle in tropical East Africa during the Paleocene–Eocene Thermal Maximum, *Palaeogeogr., Palaeoclimatol., Palaeoecol.*, *329–330*(0), 10-21, doi:10.1016/j.palaeo.2012.02.002.

Hay, W. W., et al. (1999), Alternative global Cretaceous paleogeography, *Geological Society of America Special Papers*, *332*, 1-47, doi:10.1130/0-8137-2332-9.1.

Held, I. M., and B. J. Soden (2000), Water Vapor Feedback and Global Warming, *Annual Review of Energy and the Environment*, *25*(1), 441-475, doi:doi:10.1146/annurev.energy.25.1.441.

Held, I. M., and B. J. Soden (2006), Robust Responses of the Hydrological Cycle to Global Warming, *J. Clim.*, *19*(21), 5686-5699, doi:10.1175/jcli3990.1.

Higgins, J. A., and D. P. Schrag (2006), Beyond methane: Towards a theory for the Paleocene–Eocene Thermal Maximum, *Earth Planet. Sci. Lett.*, *245*(3–4), 523-537, doi:10.1016/j.epsl.2006.03.009.

Hönisch, B., K. A. Allen, D. W. Lea, H. J. Spero, S. M. Eggins, J. Arbuszewski, P. deMenocal, Y. Rosenthal, A. D. Russell, and H. Elderfield (2013), The influence of salinity on Mg/Ca in planktic foraminifers – Evidence from cultures, core-top sediments and complementary δ18O, *Geochim. Cosmochim. Acta*, *121*(0), 196-213, doi:http://dx.doi.org/10.1016/j.gca.2013.07.028.

Huber, M., and A. Goldner (2012), Eocene monsoons, *Journal of Asian Earth Sciences*, *44*(0), 3-23, doi:http://dx.doi.org/10.1016/j.jseaes.2011.09.014.

Hupp, B. N., D. C. Kelly, J. C. Zachos, and T. J. Bralower (2019), Effects of size-dependent sediment mixing on deep-sea records of the Paleocene-Eocene Thermal Maximum, *Geology*, *47*(8), 749-752, doi:10.1130/g46042.1.

John, C. M., S. M. Bohaty, J. C. Zachos, A. Sluijs, S. Gibbs, H. Brinkhuis, and T. J. Bralower (2008), North American continental margin records of the Paleocene-Eocene thermal maximum: Implications for global carbon and hydrological cycling, *Paleoceanography*, *23*(2), PA2217, doi:10.1029/2007pa001465.

John, C. M., N. R. Banerjee, F. J. Longstaffe, C. Sica, K. R. Law, and J. C. Zachos (2012), Clay assemblage and oxygen isotopic constraints on the weathering response to the Paleocene-Eocene thermal maximum, east coast of North America, *Geology*, *40*(7), 591-594, doi:10.1130/g32785.1.

Jones, T. D., D. J. Lunt, D. N. Schmidt, A. Ridgwell, A. Sluijs, P. J. Valdes, and M. Maslin (2013), Climate model and proxy data constraints on ocean warming across the Paleocene–Eocene Thermal Maximum, *Earth-Sci. Rev.*, *125*, 123-145.

Kelly, D. C. (2002), Response of Antarctic (ODP Site 690) planktonic foraminifera to the Paleocene–Eocene thermal maximum: Faunal evidence for ocean/climate change, *Paleoceanography*, *17*(4), 1071, doi:10.1029/2002pa000761.

Kelly, D. C., J. C. Zachos, T. J. Bralower, and S. A. Schellenberg (2005), Enhanced terrestrial weathering/runoff and surface ocean carbonate production during the recovery stages of the Paleocene-Eocene thermal maximum, *Paleoceanography*, *20*(4), PA4023, doi:10.1029/2005pa001163.

Kennett, J. P., and L. D. Stott (1991), Abrupt deep-sea warming, palaeoceanographic changes and benthic extinctions at the end of the Paleocene, *Nature*, *353*, 225-229.

Kent, D. V., B. S. Cramer, L. Lanci, D. Wang, J. D. Wright, and R. Van der Voo (2003), A case for a comet impact trigger for the Paleocene/Eocene thermal maximum and carbon isotope excursion, *Earth Planet. Sci. Lett.*, *211*(1–2), 13-26, doi:http://dx.doi.org/10.1016/S0012-821X(03)00188-2.

Kiehl, J. T., C. A. Shields, M. A. Snyder, J. C. Zachos, and M. Rothstein (2018), Greenhouse- and orbital-forced climate extremes during the early Eocene, *Philosophical Transactions of the Royal Society A: Mathematical, Physical and Engineering Sciences*, *376*(2130), 20170085.

Killingley, J. S. (1983), Effects of diagenetic recrystallization on $^{18}O/^{16}O$ values of deep-sea sediments, *Nature*, *301*, 594-597.

Kirtland Turner, S., P. M. Hull, L. R. Kump, and A. Ridgwell (2017), A probabilistic assessment of the rapidity of PETM onset, *Nature Communications*, *8*.

Kita, N. T., T. Ushikubo, B. Fu, and J. W. Valley (2009), High precision SIMS oxygen isotope analysis and the effect of sample topography, *Chem. Geol.*, *264*(1-4), 43-57, doi:10.1016/j.chemgeo.2009.02.012.

Kozdon, R., T. Ushikubo, N. T. Kita, M. Spicuzza, and J. W. Valley (2009), Intratest oxygen isotope variability in the planktonic foraminifer *N. pachyderma:* Real vs. apparent vital effects by ion microprobe, *Chem. Geol.*, *258*, 327-337, doi:10.1016/j.chemgeo.2008.10.032.

Kozdon, R., D. C. Kelly, N. T. Kita, J. H. Fournelle, and J. W. Valley (2011), Planktonic foraminiferal oxygen isotope analysis by ion microprobe technique suggests warm tropical sea surface temperatures during the Early Paleogene, *Paleoceanography*, *26*(3), PA3206, doi:10.1029/2010pa002056.

Kozdon, R., D. C. Kelly, K. Kitajima, A. Strickland, J. H. Fournelle, and J. W. Valley (2013), In situ $\delta^{18}O$ and Mg/Ca analyses of diagenetic and planktic foraminiferal calcite preserved in a deep-sea record of the Paleocene-Eocene thermal maximum, *Paleoceanography*, *28*(3), 517-528, doi:10.1002/palo.20048.

Kraus, M. J., and S. Riggins (2007), Transient drying during the Paleocene–Eocene Thermal Maximum (PETM): Analysis of paleosols in the bighorn basin, Wyoming, *Palaeogeogr., Palaeoclimatol., Palaeoecol.*, *245*(3–4), 444-461, doi:10.1016/j.palaeo.2006.09.011.

Kurtz, A. C., L. R. Kump, M. A. Arthur, J. C. Zachos, and A. Paytan (2003), Early Cenozoic decoupling of the global carbon and sulfur cycles, *Paleoceanography*, *18*(4), 1090, doi:10.1029/2003pa000908.

Larrasoaña, J. C., A. P. Roberts, L. Chang, S. A. Schellenberg, J. D. Fitz Gerald, R. D. Norris, and J. C. Zachos (2012), Magnetotactic bacterial response to Antarctic dust supply during the Palaeocene–Eocene thermal maximum, *Earth Planet. Sci. Lett.*, *333–334*, 122-133, doi:http://dx.doi.org/10.1016/j.epsl.2012.04.003.

Lea, D. W., T. A. Mashiotta, and S. H.J. (1999), Controls on magnesium and strontium uptake in planktonic foraminifera determined by live culturing, *Geochim. Cosmochim. Acta*, *63*(16), 2369-2379.

Martin, P. A., and D. W. Lea (2002), A simple evaluation of cleaning procedures on fossil benthic foraminiferal Mg/Ca, *Geochemistry Geophysics Geosystems*, *3*(10).

McInerney, F. A., and S. L. Wing (2011), The Paleocene-Eocene Thermal Maximum: A Perturbation of Carbon Cycle, Climate, and Biosphere with Implications for the Future, *Annu. Rev. Earth Planet. Sci.*, *39*(1), 489-516, doi:doi:10.1146/annurev-earth-040610-133431.

Nicolo, M. J., G. R. Dickens, and C. J. Hollis (2010), South Pacific intermediate water oxygen depletion at the onset of the Paleocene-Eocene thermal maximum as depicted in New Zealand margin sections, *Paleoceanography*, *25*(4), n/a-n/a, doi:10.1029/2009PA001904.

Nürnberg, D. (1995), Assessing the reliability of magnesium in foraminiferal calcite as a proxy for water mass temperatures, *J. Foraminifer. Res.*, *25*, 350-368.

Pagani, M., N. Pedentchouk, M. Huber, A. Sluijs, S. Schouten, H. Brinkhuis, J. S. Sinninghe Damste, G. R. Dickens, and S. Expedition (2006), Arctic hydrology during global warming at the Palaeocene/Eocene thermal maximum, *Nature*, *442*(7103), 671-675, doi:http://www.nature.com/nature/journal/v442/n7103/suppinfo/nature05043_S1.html.

Pagani, M., M. Huber, and B. B. Sageman (2013), Greenhouse climates, in *Treatise on Geochemistry: Second Edition*, edited, pp. 281-304, Elsevier Inc.

Panchuk, K., A. Ridgwell, and L. R. Kump (2008), Sedimentary response to Paleocene-Eocene Thermal Maximum carbon release: A model-data comparison, *Geology*, *36*(4), 315-318, doi:10.1130/g24474a.1.

Pearson, P. N., P. W. Ditchfield, J. Singano, K. G. Harcourt-Brown, C. J. Nicholas, R. K. Olsson, N. J. Shackleton, and M. Hall (2001), Warm tropical sea surface temperatures in the Late Cretaceous and Eocene epochs, *Nature*, *413*, 481-487.

Penman, D. E., B. Hönisch, R. E. Zeebe, E. Thomas, and J. C. Zachos (2014), Rapid and sustained surface ocean acidification during the Paleocene-Eocene Thermal Maximum, *Paleoceanography*, *29*(5), 2014PA002621, doi:10.1002/2014pa002621.

Pierrehumbert, R. T. (2002), The hydrologic cycle in deep-time climate problems, *Nature*, *419*(6903), 191-198.

Pujalte, V., S. Monechi, S. Ortíz, X. Orue-Etxebarria, F. Rodríguez-Tovar, and B. Schmitz (2019), Microcodium-rich turbidites in hemipelagic sediments during the Paleocene–Eocene Thermal Maximum: Evidence for extreme precipitation events in a Mediterranean climate (Río Gor section, southern Spain), *Global Planet. Change*, *178*, 153-167.

Quillévéré, F., R. D. Norris, I. Moussa, and W. A. Berggren (2001), Role of photosymbiosis and biogeography in the diversification of early Paleogene acarininids (planktonic foraminifera):, *Paleobiology*, *27*, 311-326.

Robert, C., and J. P. Kennett (1994), Antarctic subtropical humid episode at the Paleocene-Eocene boundary: Clay-mineral evidence, *Geology*, *22*(3), 211-214, doi:10.1130/0091-7613(1994)022<0211:asheat>2.3.co;2.

Röhl, U., T. J. Bralower, R. D. Norris, and G. Wefer (2000), New chronology for the late Paleocene thermal maximum and its environmental implications, *Geology*, *28*(10), 927-930, doi:10.1130/0091-7613(2000)28<927:ncftlp>2.0.co;2.

Röhl, U., T. Westerhold, T. J. Bralower, and J. C. Zachos (2007), On the duration of the Paleocene-Eocene thermal maximum (PETM), *Geochem. Geophys. Geosyst.*, *8*(12), Q12002, doi:10.1029/2007gc001784.

Rosenthal, Y., E. A. Boyle, and N. Slowey (1997), Temperature control on the incorporation of magnesium, strontium, fluorine, and cadmium into benthic foraminiferal shells from Little Bahama Bank: Prospects for thermocline paleoceanography, *Geochim. Cosmochim. Acta*, *61*(17), 3633-3643, doi:http://dx.doi.org/10.1016/S0016-7037(97)00181-6.

Rosenthal, Y., G. P. Lohmann, K. C. Lohmann, and R. M. Sherrell (2000), Incorporation and Preservation of Mg in Globigerinoides sacculifer: Implications for Reconstructing the Temperature and 18O/16O of Seawater, *Paleoceanography*, *15*(1), 135-145, doi:10.1029/1999pa000415.

Schmitt, R. W. (1995), The ocean component of the global water cycle, *Rev. Geophys.*, *33*(S2), 1395-1409, doi:10.1029/95RG00184.

Schmitz, B., and V. Pujalte (2007), Abrupt increase in seasonal extreme precipitation at the Paleocene-Eocene boundary, *Geology*, *35*(3), 215-218, doi:10.1130/g23261a.1.

Segev, E., and J. Erez (2006), Effect of Mg/Ca ratio in seawater on shell composition in shallow benthic foraminifera, *Geochemistry, Geophysics, Geosystems*, *7*(2), n/a-n/a, doi:10.1029/2005GC000969.

Sexton, P. F., P. A. Wilson, and P. N. Pearson (2006), Microstructural and geochemical perspectives on planktic foraminiferal preservation: "Glassy" versus "Frosty", *Geochemistry Geophysics Geosystems*, *7*(12), doi:10.1029/2006GC001291.

Shackleton, N. (1967), Oxygen Isotope Analyses and Pleistocene Temperatures Re-assessed, *Nature*, *215*(5096), 15-17.

Shackleton, N. J. (1974), Attainment of Isotopic Equilibrium between Ocean Water and the Benthonic Foraminifera Genus *Uvigerina*: Isotopic Changes in the Ocean During the Last Glacial, *Colloques Internationaux du C.N.R.S.*, *219*, 203-209.

Shackleton, N. J., and J. P. Kennett (1975), Paleotemperature History of the Cenozoic and the initiation of Antarctic glaciation; Oxygen and carbon isotope analyses in DSDP Sotes 277, 279, and 281, in *Initial Reports of the Deep Sea Drilling Project*, edited by J. P. Kennett and R. E. Houtz, pp. 743-755, U.S. Government Printing Office, Washington D.C.

Sluijs, A., et al. (2006), Subtropical Arctic Ocean temperatures during the Palaeocene/Eocene thermal maximum, *Nature*, *441*(7093), 610-613, doi:http://www.nature.com/nature/journal/v441/n7093/suppinfo/nature04668_S1.html.

Sluijs, A., U. Röhl, S. Schouten, H.-J. Brumsack, F. Sangiorgi, J. S. Sinninghe Damsté, and H. Brinkhuis (2008), Arctic late Paleocene - early Eocene paleoenvironments with special emphasis on the Paleocene-Eocene thermal maximum (Lomonosov Ridge, Integrated Ocean Drilling Program Expedition 302), *Paleoceanography*, *23*(1), PA1S11, doi:10.1029/2007pa001495.

Sluijs, A., P. K. Bijl, S. Schouten, U. Röhl, G. J. Reichart, and H. Brinkhuis (2011), Southern ocean warming, sea level and hydrological change during the Paleocene-Eocene thermal maximum, *Clim. Past*, *7*(1), 47-61, doi:10.5194/cp-7-47-2011.

Spero, H. J., J. Bijma, D. W. Lea, and B. E. Bemis (1997), Effect of seawater carbonate concentration on foraminiferal carbon and oxygen isotopes, *Nature*, *390*(6659), 497-500.

Svensen, H., S. Planke, A. Malthe-Sorenssen, B. Jamtveit, R. Myklebust, T. Rasmussen Eidem, and S. S. Rey (2004), Release of methane from a volcanic basin as a mechanism for initial Eocene global warming, *Nature*, *429*(6991), 542-545.

Thiry, M. (2000), Palaeoclimatic interpretation of clay minerals in marine deposits: an outlook from the continental origin, *Earth-Sci. Rev.*, *49*, 201-221.

Thomas, D. J., T. J. Bralower, and J. C. Zachos (1999), New evidence for subtropical warming during the late Paleocene thermal maximum: Stable isotopes from Deep Sea Drilling Project Site 527, Walvis Ridge, *Paleoceanography*, *14*(5), 561-570.

Thomas, D. J., J. C. Zachos, T. J. Bralower, E. Thomas, and S. Bohaty (2002), Warming the fuel for the fire: Evidence for the thermal dissociation of methane hydrate during the Paleocene-Eocene thermal maximum, *Geology*, *30*, 1067-1070.

Thomas, E. (1990), Late Cretaceous through Neogene deep-sea benthic foraminifers (Maud Rise, Weddell Sea, Antarctica), *Proceedings of the Ocean Drilling Program, Scientific Results*, *113*.

Tipple, B. J., M. Pagani, S. Krishnan, S. S. Dirghangi, S. Galeotti, C. Agnini, L. Giusberti, and D. Rio (2011), Coupled high-resolution marine and terrestrial records of carbon and hydrologic cycles variations during the Paleocene–Eocene Thermal Maximum (PETM), *Earth Planet. Sci. Lett.*, *311*(1–2), 82-92, doi:10.1016/j.epsl.2011.08.045.

Uchikawa, J., and R. E. Zeebe (2010), Examining possible effects of seawater pH decline on foraminiferal stable isotopes during the Paleocene-Eocene Thermal Maximum, *Paleoceanography*, *25*(2), PA2216, doi:10.1029/2009pa001864.

Valley, J. W., and N. T. Kita (2009), *In situ* oxygen isotope geochemistry by ion microprobe, in *MAC Short Course: Secondary Ion Mass Spectrometry in the Earth Sciences*, edited by M. Fayek, pp. 16-63.

Wing, S. L., G. J. Harrington, F. A. Smith, J. I. Bloch, D. M. Boyer, and K. H. Freeman (2005), Transient Floral Change and Rapid Global Warming at the Paleocene-Eocene Boundary, *Science*, *310*(5750), 993-996, doi:10.1126/science.1116913.

Zachos, J. C., M. Pagani, L. Sloan, E. Thomas, and K. Billups (2001), Trends, Rhythms, and Aberrations in Global Climate 65 Ma to Present., *Science*, *292*, 686-693, doi:10.1126/science.1059412.

Zachos, J. C., M. W. Wera, S. Bohaty, M. L. Delaney, M. R. Petrizzo, A. Brill, T. J. Bralower, and I. Premoli-Silva (2003), A transient rise in tropical sea surface temperature during the Paleocene-Eocene Thermal Maximum, *Science*, *302*, 1551-1554, doi:10.1126/science.1090110.

Zachos, J. C., et al. (2005), Rapid Acidification of the Ocean During the Paleocene-Eocene Thermal Maximum, *Science*, *308*(5728), 1611-1615, doi:10.1126/science.1109004.

Zachos, J. C., S. Schouten, S. Bohaty, T. Quattlebaum, A. Sluijs, H. Brinkhuis, S. J. Gibbs, and T. J. Bralower (2006), Extreme warming of mid-latitude coastal ocean during the Paleocene-Eocene Thermal Maximum: Inferences from TEX$_{86}$ and isotope data, *Geology*, *34*(9), 737-740, doi:10.1130/G22522.1.

Zachos, J. C., G. R. Dickens, and R. E. Zeebe (2008), An early Cenozoic perspective on greenhouse warming and carbon-cycle dynamics, *Nature*, *451*, 279-283, doi:10.1038/nature06588.

Zeebe, R. E., J. C. Zachos, K. Caldeira, and T. Tyrrell (2008), Carbon Emissions and Acidification, *Science*, *321*(5885), 51-52, doi:10.1126/science.1159124.

Zeebe, R. E., J. C. Zachos, and G. R. Dickens (2009), Carbon dioxide forcing alone insufficient to explain Palaeocene-Eocene Thermal Maximum warming, *Nature Geoscience*, *2*, 576-580, doi:10.1038/NGEO578.

Zeebe, R. E., and J. C. Zachos (2013), *Long-term legacy of massive carbon input to the Earth system: Anthropocene versus Eocene*.

Zeebe, R. E., and L. J. Lourens (2019), Solar System chaos and the Paleocene–Eocene boundary age constrained by geology and astronomy, *Science*, *365*(6456), 926-929, doi:10.1126/science.aax0612.

Zhang, Q., L. Ding, K. Kitajima, J. W. Valley, B. Zhang, X. Xu, H. Willems, and A. Klügel (2020), Constraining the magnitude of the carbon isotope excursion during the Paleocene-Eocene thermal maximum using larger benthic foraminifera, *Global Planet. Change*, *184*, 103049.
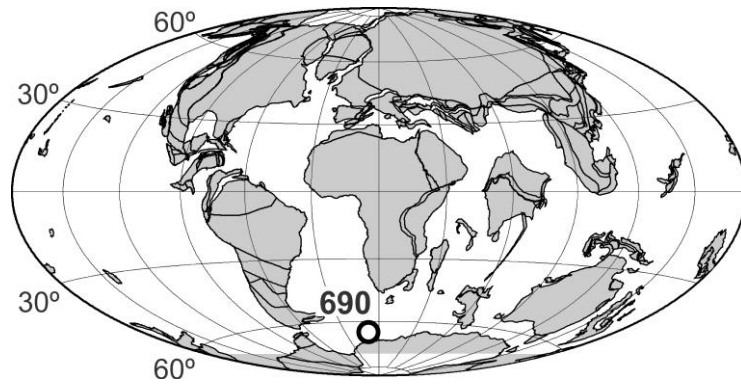
Fig. 1. Early Eocene paleogeography and location of Site 690, Weddell Sea (map modified from the Ocean Drilling Stratigraphic Network, ODSN, compiled using data files from (Hay et al., 1999)).
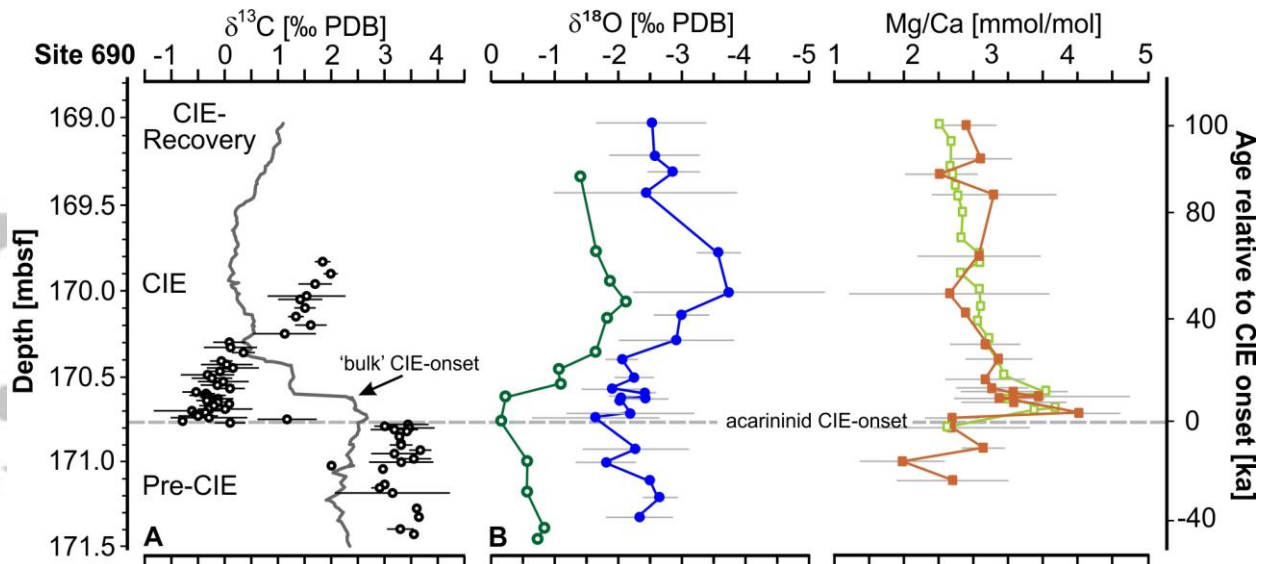
Fig. 2. Parallel chemostratigraphies for the Site 690 PETM section. Data plotted against core depth (meters below seafloor, mbsf) and relative (± ka) to CIE onset in the planktic foraminifer (acarininid) $\delta^{13}C$ record. (**A**) Bulk-carbonate (solid line) and acarininid (open circles) $\delta^{13}C$ records of the carbon isotope excursion (CIE). Acarininid record constructed using mean values of published (Thomas et al., 2002) single-shell data, error bars represent ±2 SEM for each sample. Note: acarininid shells displaced by sediment mixing were excluded, and CIE onset in bulk-carbonate record occurs 14 cm above its position in the acarininid record (Hupp et al., 2019). (**B**) Parallel planktic foraminifer $\delta^{18}O$ records, one constructed with *in situ* SIMS values (blue, filled circles) and the other with values obtained by conventional multi-shell acid solution techniques (green, open circles) (Kennett and Stott, 1991). Error bars in the SIMS-based $\delta^{18}O$ record represent ±2 SEM for each sample. (**C**) Complementary acarininid Mg/Ca ratio records, one constructed with *in situ* EPMA values (brown, filled squares, with error bars connoting ±2 SEM for each sample) and the other with values obtained by conventional, multi-shell ICP-MS analysis (light green, open squares). Error bars on *in situ* values are large due to inter- and intrashell variability in Mg/Ca; however, average values for each core sample delineate the same trends as conventional, multi-shell ICP-MS measurements.
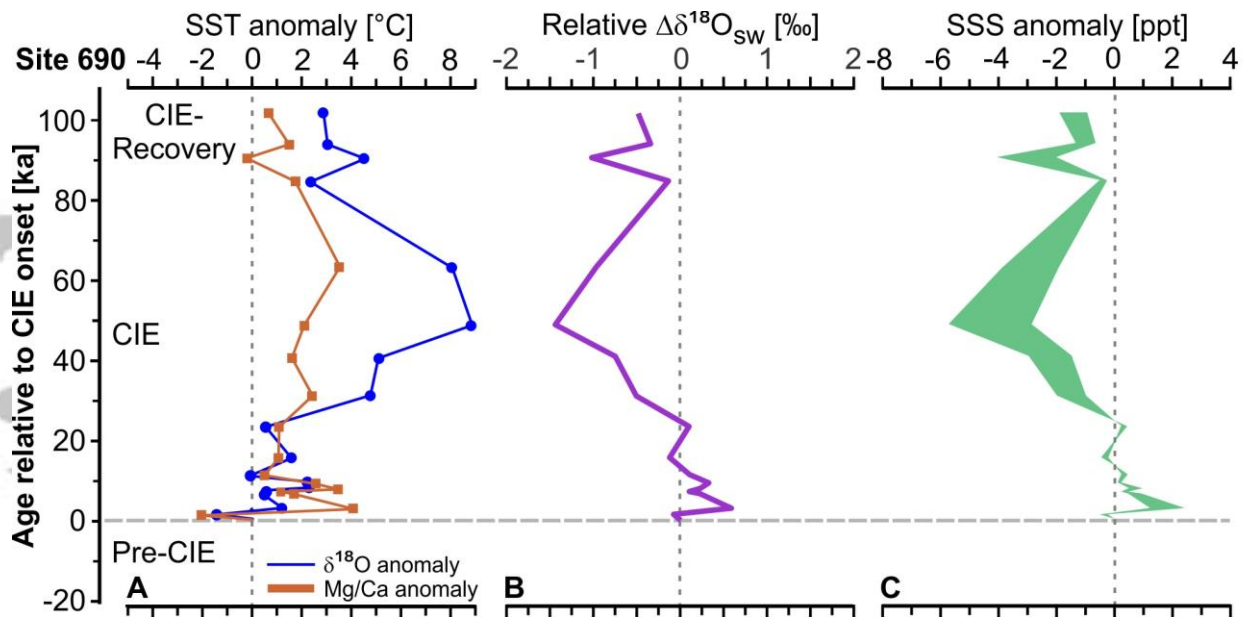
Fig. 3. Secular variation in sea-surface properties during the PETM at Site 690 as expressed relative to pre-CIE background conditions. (**A**) Parallel sea-surface temperature anomaly records constructed with planktic foraminifer *in situ* $\delta^{18}O_{SIMS}$ data assuming a constant $\delta^{18}O_{sw}$ value (blue), and *in situ* Mg/Ca measurements (brown). The $\delta^{18}O_{SIMS}$ anomaly record corrected for pH drop that occurred after the CIE onset, and the Mg/Ca anomaly record is adjusted for lower Eocene seawater Mg/Ca, pH, and salinity (see Section 2.5. for more details). (**B**) Changes in $\delta^{18}O_{sw}$ computed using the differences between the $\delta^{18}O_{SIMS}$ SST anomaly record and the Mg/Ca SST anomaly record. (**C**) Sea-surface salinity anomalies relative to the pre-CIE baseline calculated using a range of $\Delta\delta^{18}O_{sw}/\Delta$salinity relations (0.5‰/salinity unit and 0.25‰/salinity unit). Horizontal dashed line (gray) = CIE onset in acarininid $\delta^{13}C$ record. Vertical dashed lines (gray) = mean baseline for pre-CIE background values.